1   *Article*

2   # A Machine Learning Approach for the Discovery of
3   # Ligand-specific Functional Mechanisms of GPCRs

4   **Ambrose Plante [1], Derek M. Shore[1], Giulia Morra[1], George Khelashvili[1,2] and Harel**
5   **Weinstein[1,2,*])**

6   [1]   Weill Cornell Medical College, Department of Physiology and Biophysics; agp2004@med.cornell.edu
7   (A.P.); des2037@med.cornell.edu (D.M.S.); gim2010@med.cornell.edu (G.M.)
8   [2]   Weill Cornell Medical College, Department of Physiology and Biophysics & Institute for Computational
9   Biomedicine; gek2009@med.cornell.edu (G.K.)
10   *   Correspondence: haw2002@med.cornell.edu; Tel.: +1-212-746-6358 (H.W.)

12   **Abstract: G protein-coupled receptors (**GPCRs) play a key role in many cellular signaling
13   mechanisms, and must select among multiple coupling possibilities in a ligand-specific manner in
14   order to carry out a myriad of functions in diverse cellular contexts. Much has been learned about
15   the molecular mechanisms of ligand-GPCR complexes from Molecular Dynamics (MD) simulations.
16   However, to explore ligand-specific differences in the response of a GPCR to diverse ligands, as is
17   required to understand ligand bias and functional selectivity, necessitates creating very large
18   amounts of data from the needed large-scale simulations. This becomes a Big Data problem for the
19   high dimensionality analysis of the accumulated trajectories. Here we describe a new machine
20   learning (ML) approach to the problem that is based on transforming the analysis of GPCR function-
21   related, ligand-specific differences encoded in the MD simulation trajectories into a representation
22   recognizable by state-of-the-art deep learning object recognition technology. We illustrate this
23   method by applying it to recognize the pharmacological classification of ligands bound to the 5-
24   HT_{2A} and D2 subtypes of class A GPCRs from the serotonin and dopamine families. The ML-based
25   approach is shown to perform the classification task with high accuracy, and we identify the
26   molecular determinants of the classifications in the context of GPCR structure and function. This
27   study builds a framework for the efficient computational analysis of MD Big Data collected for the
28   purpose of understanding ligand-specific GPCR activity.

29   **Keywords:** Functional selectivity; Biased ligands; Molecular Dynamics; Deep Neural Networks;
30   Sensitivity analysis; Pharmacological efficacy;

31

32   **1. Introduction**

33   As our perception of G Protein-Coupled Receptors (GPCRs) evolve from simple on/off switches
34   to multistate microprocessors [1], new questions arise regarding the complexity and specificity of
35   GPCR signaling. A major reason for seeking this deeper understanding is the quest for information
36   in support of rational design of more efficacious and specific drugs that exert their effects by targeting
37   GPCRs.
38   As GPCRs are often the main drivers and regulators of signaling into the cell, they must be able
39   to select among multiple signaling pathways based on the stimulus they receive for action. The ability
40   of different ligands to elicit such differential signaling is commonly referred to as *functional selectivity*
41   of the receptor, or *biased agonism*. For specific subtypes of serotonin (5-hydroxytriptamine; 5-HT)
42   receptors, Berg and colleagues [2] demonstrated that such biased signaling occurs through ligand-
43   dependent coupling to G_q or G_i proteins. For other class A GPCRs, biased agonism involves a
44   selection between G protein and arrestin-coupled pathways. The notion that functional selectivity
45   results from differences in receptor conformation arising from differential ligand-receptor
46   interactions was proposed as soon as the dynamics of ligand-receptor complexes demonstrated the

complexity of receptor activation [3-5]. Furthermore, additional structural evidence for distinct receptor conformations of angiotensin receptors activated by different ligands exhibiting functional selectivity has been reported [6]. How a given ligand influences a receptor's conformational ensemble remained enigmatic in spite of observations of differences in some elements of the structural dynamics of receptors exhibiting functional selectivity, including the 5-HT$_{2A}$ receptor [7].

Molecular Dynamics (MD) has proven to be a powerful tool for understanding protein function at the molecular level [8-11], and could deliver much-needed insight into developing a theory of functional selectivity at GPCRs. Notably, however, an MD study of functional selectivity would require many trajectories of GPCR-ligand complexes from extensive sets of ligands from each functionally-selective class in order to understand this allosteric phenomenon [12]. Furthermore, previous studies by Wingler *et al.* [6] suggest that the differences among the various ligand-dependent receptor conformations may be subtle. Thus, analyzing the MD data to gain insights into functional selectivity will require finding a low-density signal (i.e., detectable only after analyzing a lot of data) in a huge dataset, a common problem in the analysis of Big Data. Although there is no formally accepted definition of Big Data, it is generally referred to as "datasets that could not be perceived, acquired, managed, and processed by traditional [Information Technology] and software/hardware tools within a tolerable time" [13]. Concordantly, analyzing MD simulations of very large scale remains a challenge and an open area of research. As discussed by Frankel and Reid [14], finding new ways to represent and interpret Big Data may allow us to explore new questions and extract new meaning from our research. These new representations must be efficient enough to process the data in a "tolerable" amount of time, and must be able to encode the relationship between the conformational details and functional properties of the molecules being studied.

The new frontier of analyzing Big Data lies in the field of machine learning (ML). Companies such as Facebook and Google, as well as academia (e.g., Massachusetts Institute of Technology), have already made great progress in this realm. For example, their algorithms excel at differentiating between highly similar objects, or identifying the same object in distinct states. Specifically, deep neural networks (DNNs) have already been shown to classify pixel representations of objects (pictures) with near-perfect accuracy[15]. The strengths of DNNs lie in their ability to find complex, non-linear patterns within data sets that may be too large and high dimensional for a human to analyze, or for which a model does not yet exist. It is reasonable, therefore, to consider the application of this class of approaches to the Big Data problem presented by the application of MD simulations to the analysis of GPCR mechanisms.

The aforementioned difficulties in identifying conformational ensemble differences in GPCRs attributable to the binding of various ligands, fall into both categories: the MD trajectories are too large and high dimensional to characterize manually, and there does not exist a sufficient structure/dynamics-based model of functional selectivity in which to understand them. Therefore, in order to use MD to advance such an understanding, we set out to transform the problem of identifying functional differences encoded in different structures, as they are visited by MD trajectories, into a representation recognizable by state-of-the-art object recognition technology. Since the effect of ligand binding to a functional site is the result of allosteric mechanisms [12, 16, 17] that alter the energetic landscape of the targeted protein, this new representation must differentiate between ensembles of ligand-dependent protein conformations. In GPCRs, information about the binding of ligands in either the orthosteric or allosteric sites is transferred through the receptor along allosteric pathways to a functional site on the protein [17]. It is reasonable, therefore, that in comparing ensembles of ligand-dependent conformations, these differences may involve only a small subset of residues. Consequently, in order to understand the molecular mechanism of protein function, we must be able to identify the motifs of the protein (residues/atoms) that undergo conformational rearrangements pertaining to ligand-specific functional states. The collection of these important motifs are known as Collective Variables (CVs). The identification of these CVs within the low-density signal of large-scale data is a challenging problem, but one which object-recognition technology is designed to tackle.

98   To help achieve this goal of identifying the determinant motifs for the classification of
99 ligand-specific functional responses of the receptor, using an ML approach, we developed the
100 algorithm described here that transforms MD trajectories into a representation readable by state-of-
101 the-art object recognition technology. This representation is fed into a pipeline that uses a Deep
102 Neural Network (DNN) to (i)-recognize ensembles of molecular conformations and (ii)-predict
103 ligand-determined class according to structural differences learned from training. This pipeline then
104 probes the DNN to identify CVs that are discriminative between the functional states of the receptor
105 determined by the molecule being studied. We show how the results of this probing are then
106 interpreted in the context of the molecular structure of the GPCR and its dynamic properties. To
107 illustrate the application of this analysis pipeline, we present here its application to MD simulations
108 of ligand-GPCR complexes in two receptor families, the serotonin receptor subtype 2A (5-HT$_{2A}$R) and
109 the dopamine receptor subtype D2 (D2R) bound to full, partial, and inverse agonists – a well--
110 characterized pharmacological classification of receptor responses to ligands –, that is expected to be
111 recognized by the DNN.

2. Results

2.1. Transformation of MD trajectories into pixel representations readable by DNNs

114   To apply image-recognition (picture-recognition) technology in the analysis of the MD
115 trajectories for the various ligand-GPCR complexes, the complete MD trajectory for each complex
116 must be transformed into a pixel representation that constitutes the canonical input for these ML
117 algorithms. We developed a transformation that takes advantage of the similarities between the
118 components of proteins and picture representations: both are composed of bits of information, *i.e.*,
119 the pixels in a picture and the atom in a protein. The definition of pixels in terms of their values of
120 red, green, and blue (RGB) parallels the definition of the individual atoms by their coordinates X, Y,
121 and Z (XYZ). Consequently, a unique representation of the protein as a picture is obtained when each
122 atom of the protein is transformed into a pixel with an RGB value that corresponds to that atom's
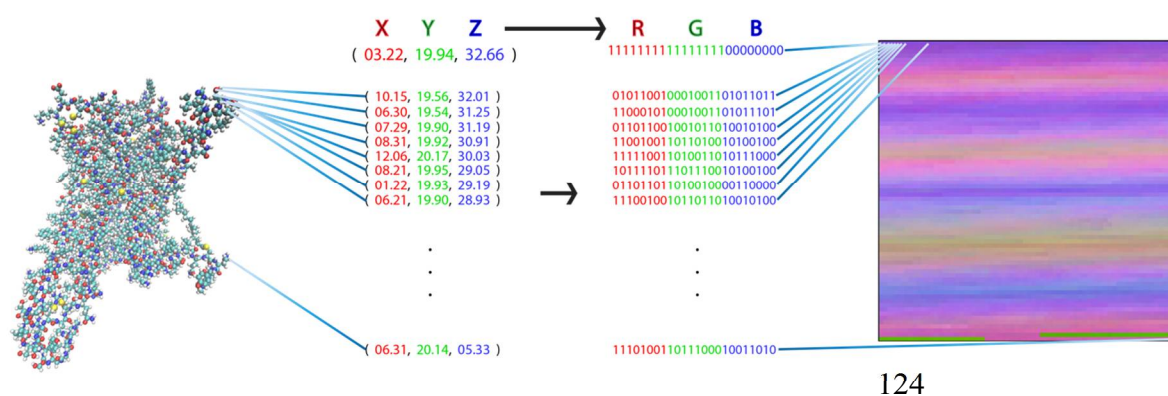123 XYZ value (**Figure 1**).

124

Figure 1: **Visual representation of a molecular structure.** Each atom of the molecule (left) is identified by the set
of (x,y,z) coordinates as illustrated by the numerical set. The transformation to a 2D picture-like representation
is obtained by assignment to each pixel representing an atom (in sequential order from top left to bottom right)
by a pixel whose RGB value is the XYZ coordinate of the atom it represents (identified by the set of digital
values). This representation has the special property that each pixel (*i.e.* matrix element) always represents the
same atom in each frame from the trajectory of a particular protein.

131 Since this procedure is sensitive to the translational and rotational movements of the protein, the
132 trajectories are pre-processed by scrambling to remove bias from the original trajectory (see the next
133 section for details on the scrambling procedure).

134

135   *2.2. Training and application of DNNs able to recognize ligand-dependent receptor conformations*

136   *2.2.1 General Protocol*

137   The representation of a protein according to the rules described in section 2.1, above, encodes the
138   three-dimensional structure of a molecule into a two dimensional picture that can be fed directly into
139   an ML algorithm, such as the convolutional neural network utilized here, without any loss of
140   information (clearly, such a loss would occur if a conventional projection-like "picture" was taken of
141   the molecule). In the method of analysis presented here, this transformation is applied to each frame
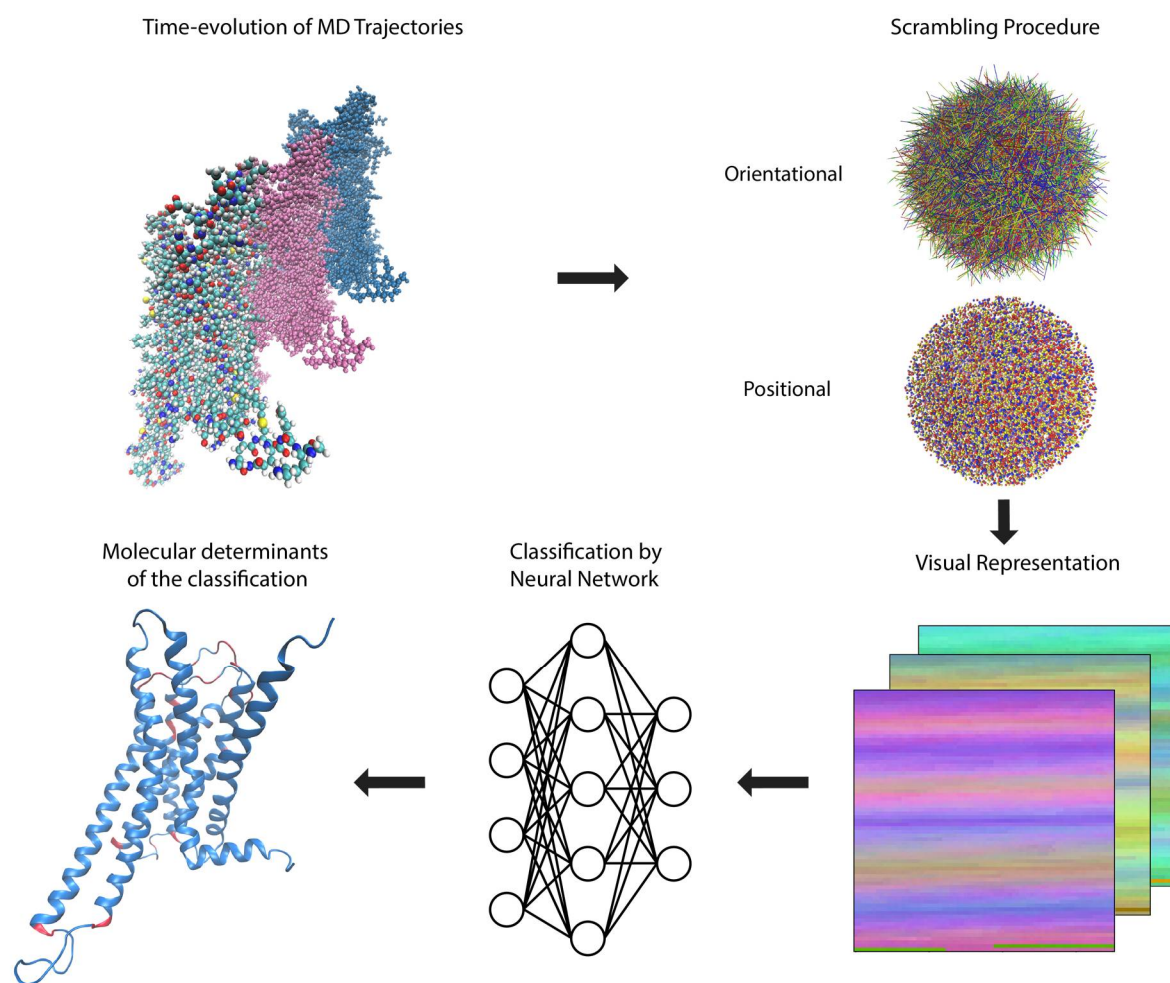142   of the MD trajectory sequentially, and followed by the steps depicted in **Figure 2**.

143

144   **Figure 2: Overview of the computer-aided inspection pipeline described in detail in the text.** MD trajectories
145   representing the time evolution of each system are subjected to a scrambling procedure to erase positional and
146   orientational information and then each frame is converted into a visual representation suitable for feeding to a
147   deep convolution neural network for training, validation, and testing of classification accuracy. A sensitivity
148   analysis protocol is carried out to reveal the most important parts of the molecule (highlighted in red, see text
149   and subsequent figures for more details) used in the classification by the neural network, and collective variables
150   are extracted from the network to aid in further analysis.

151   The trajectories collected from MD simulations of ligand-GPCR complex of the serotonin 5-
152   HT$_{2A}$R and dopamine D2R (see Methods for details) were used to illustrate the application of the
153   pipeline described in Figure 2. The data submitted for the DNN contains the coordinates of the atoms
154   in the receptor structures sampled at the time-steps of the MD trajectories (frames), presented in the
155   form of the visual representation of these coordinates (**Figure 1**), as well as the corresponding class
156   label for each structure (*i.e.* bound to agonist, partial agonist, or inverse agonist).

157   The scrambling protocol applied to the data prior to submission to the neural network (NN) is
158   an unbiasing step in which the position of each frame and its orientation are scrambled (randomly;
159   see **Figure 3** for more information on the trajectory scrambling). This is undertaken in order to
160   eliminate from consideration by the NN of any differences among frames that originate not from the
161   time-dependent molecular dynamics, but from changes in position or orientation of the ligand-GPCR
162   complex. Thus, the scrambling directs the NN algorithm to consider only the intramolecular changes
163   of the protein induced by the ligands. This scrambling is introduced in our protocol to achieve the
164   same unbiasing that is attained in image classification tasks by random orientation of objects in
165   pictures (which forces the object recognition neural networks to understand the shapes and colors of
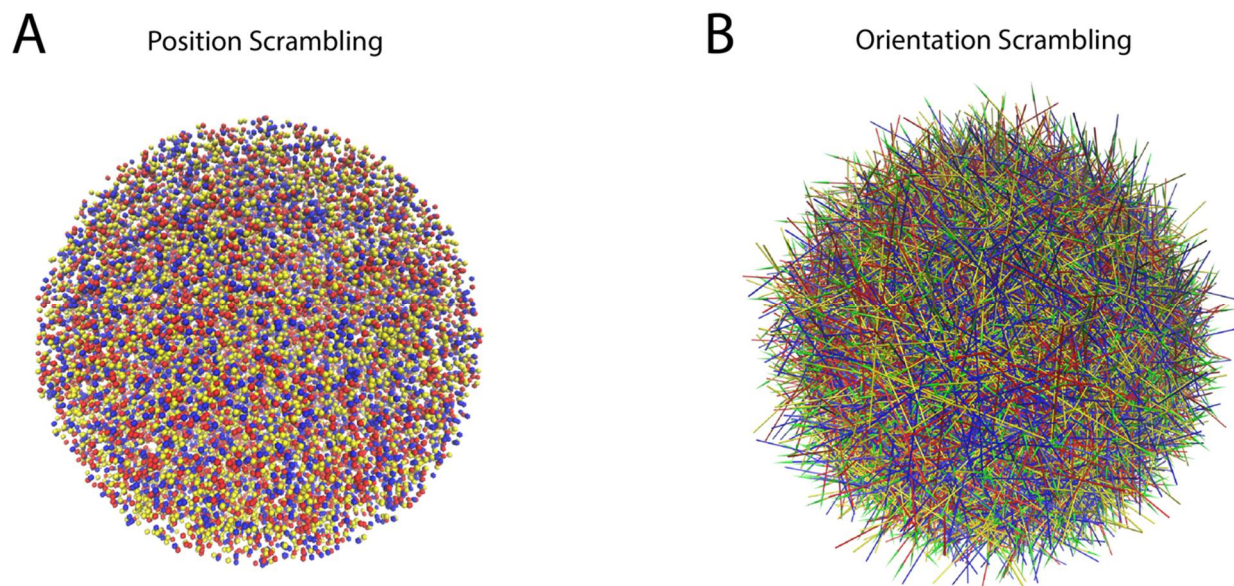166   objects, independent of their background and orientation).

167

168   **Figure 3: Illustration of the protocol for scrambling the frames of the MD trajectories**. Each frame of each
169   trajectory was <u>positionally</u> scrambled by moving its center of mass to a randomly sampled coordinate within a
170   sphere of diameter 90 Å (the size of the largest dimension of the receptor). The <u>orientation</u> of the receptor was
171   scrambled by aligning a vector defined by two arbitrarily chosen atoms (preferably on an axis connecting the
172   intracellular and extracellular ends of the GPCR) to a random unit vector in spherical coordinates. (Note: for the
173   5-HT2AR, the two atoms chosen were atoms 3695 and 4346, which are the *eta* hydrogen (H η) of K6.32 and one
174   of the *delta* hydrogens (Hδ) of L7.34, respectively) **A.** Illustrates the arbitrary positioning in space of the frames
175   belonging to different trajectories by showing the center of mass of the first 1000 frames of arbitrarily-chosen
176   trajectories from each class. Frames from a full agonist-bound trajectory are in blue, from partial agonist-bound
177   are yellow, from inverse agonist-bound are red **B.** Illustrates the arbitrary orientation of the frames from the
178   different trajectories: Green-tipped arrows with shafts going through atoms 3695 and 4346 are colored by the
179   same color scheme as in A, and drawn for each of the first 1000 frames of the same trajectories as in panel **A**.

180   The convolution neural network **(Figure 2)** was trained on training and validation sets, and
181   tested on the data set, following known ML protocols [15, 18] (see below, section 2.2.2). The results
182   for the 5-HT2AR (section 2.2.2) and D2R (section 2.2.3) systems were then analyzed as described below
183   in section 3 to identify the molecular determinants of the classification.

184

185   2.2.2 *Pharmacological classification of the MD trajectories of 5-HT2AR-ligand complexes*

186   The set of 5-HT2AR-bound pharmacologically distinct ligands chosen for this illustrative
187   application includes the full agonist serotonin (5-HT), the inverse agonist ketanserin (KET), and three
188   partial agonists of differing efficacies (LSD, DOI, LIS) of which two are similar in molecular size (L-

189 lysergic acid diethyl amide, LSD, and lisuride (LIS), and one is smaller, similar in size to 5-HT (2,5-
190 Dimethoxy-4-iodoamphetamine, DOI). The data set consists of 43,565 structures sampled with a 0.2
191 ns time-interval from the full and inverse agonist trajectories, and a 0.6 ns time-interval from the
192 partial agonist trajectories (to maintain a balance in the number of samples from each class). The
193 complete set of trajectory data, along with their corresponding class labels, was split into training,
194 validation, and test sets of size 24396, 10456, and 8713, respectively.

195   The 5-HT$_{2A}$R complexes were subjected to the general protocol described in section 2.2.1 above.
196 The results for the 5-HT$_{2A}$R test set quantify the accuracy of the neural network in predicting the class
197 labels of pharmacological classifications of the 5-HT$_{2A}$R ligands in the form of a confusion matrix
198 (**Figure 4**). The formulation of the confusion matrix relates the predicted class label of the test set
199 instances to their true class label. Each element of the confusion matrix is calculated as:

200 $$C_{(i,j)} = \sum_{n=1}^{N} F_{n,(i,j)} \quad ; \quad where \; F_{n,(i,j)} = \begin{cases} 1, & T_n = i \; AND \; P_n = j \\ 0, & otherwise \end{cases} \tag{1}$$

201 where $C_{(i,j)}$ is the (row, column) index of the confusion matrix, N is the number of instances in the
202 test set, T_n is the true class label of instance n, and P_n is the class label of instance n predicted by
203 the neural network. Each element is then normalized to the total number of instances in each class.

204   Results from the application of the analysis to the test set for the 5-HT$_{2A}$R are presented in the
205 *confusion matrix* in both numerical and a color-coded visual form **Figure 4A**. The diagonal elements
206 represent the fraction of instances for which the neural network had correctly identified the class
207 label. Off-diagonal elements show the fraction of incorrectly labeled instances and identify the class
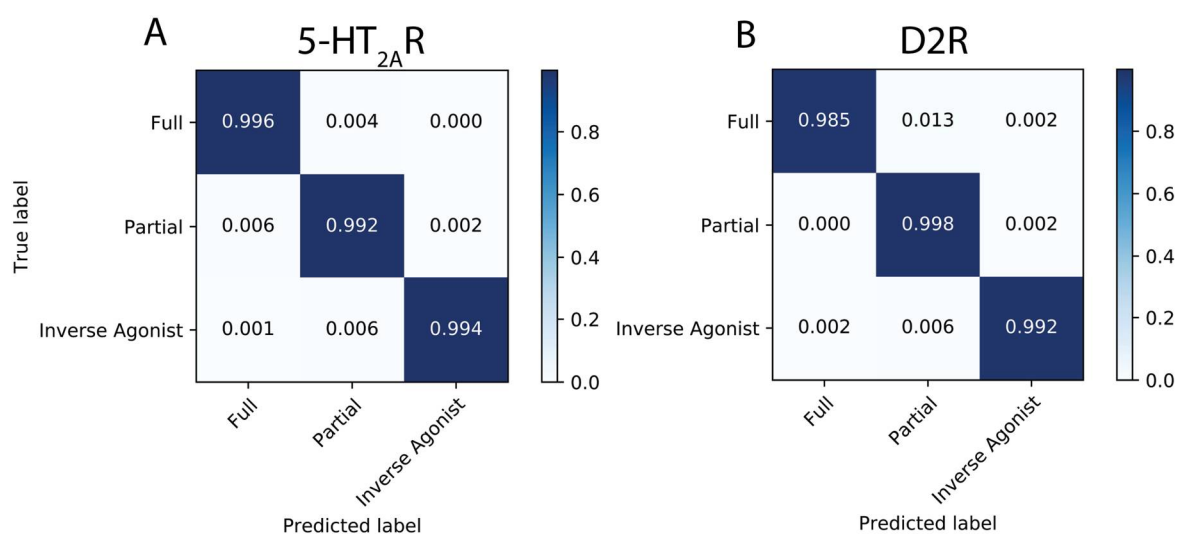208 to which they were incorrectly attributed.

209

210 **Figure 4: Results of the classification for the test set of the 5-HT$_{2A}$R (A), and D2R (B).** The coded coloring and
211 numbers show the proportion of times the neural network predicted correctly a class label (diagonal elements),
212 and the extent to which it failed to correctly predict the class label (off-diagonal elements) by confusing it with
213 another class.

214   In this illustration of the method for the 5-HT$_{2A}$R, >99% of the frames in the test set were correctly
215 labeled (the diagonal of the confusion matrix in Figure 4A). This near-perfect accuracy achieved on
216 the test set suggests that the neural network is able to recognize and classify the ligand-dependent
217 receptor conformations presented by this data set, with most of the very few incorrectly labeled
218 instances (the off-diagonal elements) involving confusion of partial agonist labels. The molecular
219 determinants for this recognition are discussed in section 2.3.

220   *2.2.3 Pharmacological classification of D2R-ligand trajectories*

221   In order to test the generalizability of the method to MD trajectories of other GPCRs, we analyzed
222   trajectories of another class A GPCR, the D2R, bound to pharmacologically distinct ligands, namely
223   the full agonist (Dopamine, DA), inverse agonist (Sulpiride, SLP), and partial agonist (Aripiprazole,
224   ARI).

225   Following the same steps described above for the analysis of 5-HT₂ₐR, the D2R trajectories (see
226   Methods) were subjected to the protocol described in section 2.2.1 above. The visual representations
227   of the coordinates from structures (frames) sampled every 0.4 ns from the trajectories of the ligand-
228   D2R complexes were randomly split into training, validation, and test sets of size 20017, 8580, and
229   7150, respectively. The accuracy of the neural network in predicting the class labels of the D2R ligands
230   in the test set is presented in **Figure 4B** as a confusion matrix (see Eq. 1 and section 2.2.2 for details
231   on how the confusion matrix was constructed). The same high accuracy achieved by the neural
232   network for the classification of the 5-HT₂ₐR trajectories, is attained in the classification of the smaller
233   set of classes for the D2R system.

234   *2.3 Identifying the molecular determinants of the classification*

235   *2.3.1 General Protocol*

236   To reveal the identity of the molecular features that were most instrumental in the classification
237   decisions of the NN, we employ a sensitivity analysis approach in the category of visual saliency [19].
238   This sensitivity analysis is based on computing the gradient of the neural network's classification
239   score for a particular label (*i.e.*, how likely the network believes a picture to be in each class), with
240   respect to each of the pixels of the input image. The higher the gradient for a particular pixel, the
241   more attention the neural network paid to it in making the classification.

242   **Figure 5** shows an example of this type of sensitivity analysis applied to a traditional image
243   classification. Here a deep neural network has correctly labeled a picture as "dog", and the part of
244   the picture that the DNN utilized to make the classification is highlighted in the heat map (also called
245   "attention map") next to it that color-codes the magnitude of the gradient for each pixel. Clearly, the
246   attention map in **Figure 5** highlights (in the collection of highest gradient values) the pixels that
247   correspond to the dog, designating them as those having been the most important pixels for
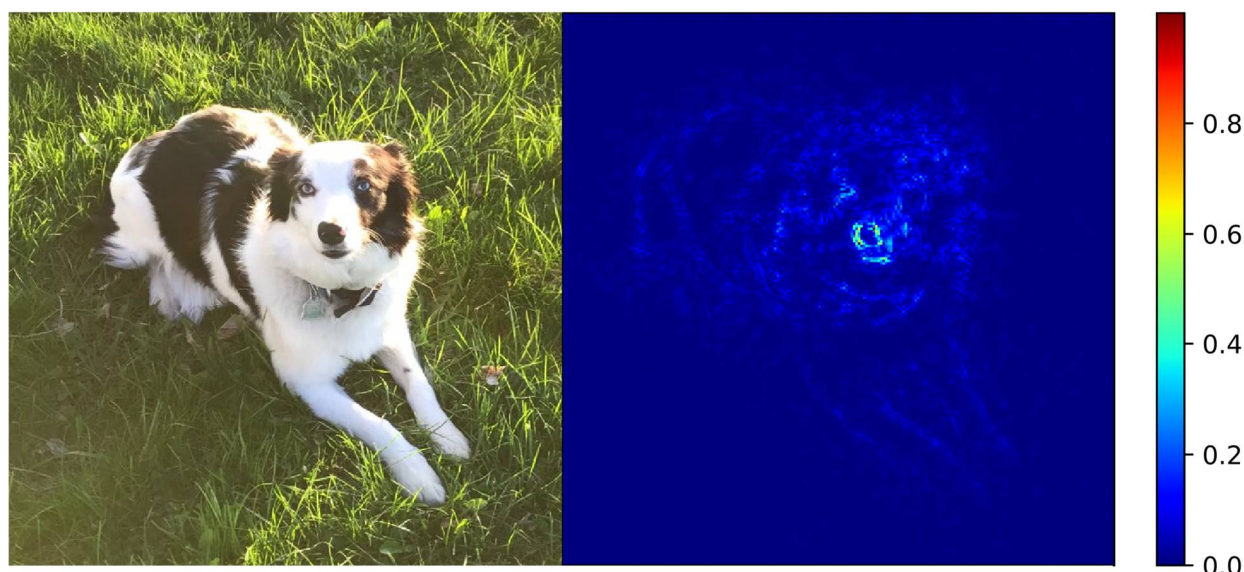248   classifying the picture correctly.

249

250

251 **Figure 5: Sensitivity analysis applied to an image of a dog**. For the heat map (attention map) on the right the
252 color bar quantifies the gradient of each pixel with respect to how likely the neural network considers this image
253 to be of a dog. This highlights the pixels that the neural network considered to be the most important for the
254 classification of the picture. The pixels that correspond to the outline of the dog are seen to be the most important
255 for the classification and thus have the highest gradient.

256

257 *2.3.1 Application to the sensitivity analysis to the 5-HT$_{2A}$R classifications*

258   We applied this sensitivity analysis approach to identify the features used by the NN to classify
259 correctly the test frames as those corresponding to the 5-HT$_{2A}$R bound to a full agonist. **Figure 6A**
260 shows an *attention map* calculated from the ligand-bound 5-HT$_{2A}$R test set. This attention map was
261 obtained by averaging the attention maps of 1000 instances (trajectory frames) of the full agonist
262 bound 5-HT$_{2A}$R. In this panel, the protein is represented by a 71x71 pixel matrix containing the atoms
263 of the receptor protein (20 atoms are missing from the C terminus) and constructed as described in
264 **Figure 1**. The elements are colored according to the color scheme with the largest gradient value
265 representing the highest importance of the atom in the classification task. The calculation of the
266 average takes advantage of the property of the visual representation of the protein in which each
267 pixel always represents the same atom.

268   To be able to relate the contributions of the identified key atoms and groups in the context of
269 structural regions of the protein, we show in **Figure 6B** the same data as in the attention map (panel
270 6A), but in a different representation in which all the pixels (*i.e.*, atoms) are listed on the X axis
271 sequentially, labeled with their generic numbering that identifies the TM segments of the GPCR
272 protein. Applying to Figure 6B an importance cutoff value of 0.15 (chosen by inspection of the
273 attention map), the residues considered to be most important in the classification of the ligand bound
274 to the receptor are found to reside in the middle and the extracellular ends of TMs 2-5 (positions 2.56,
275 2.65, 3.28, 4.58, 4.59, 4.62, 4.63, 4.67, and 5.35-5.37, residues labeled with the generic Ballesteros-
276 Weinstein numbering[20]), at the intracellular ends of TMs 2 and 3 (positions 2.38 and 3.55) and in the
277 extracellular loops ECL1 and ECL2, as well as intracellular loops ICL2 and ICL3 (the pieces of which
278 that were identified as important exchange between loop and helical extensions of TM5 and TM6
279 throughout the trajectories). There is a roughly even distribution between important residues that
280 reside in the loops and the helices. These sites are indicated on the 5-HT$_{2A}$R structure in **Figure 6C**.
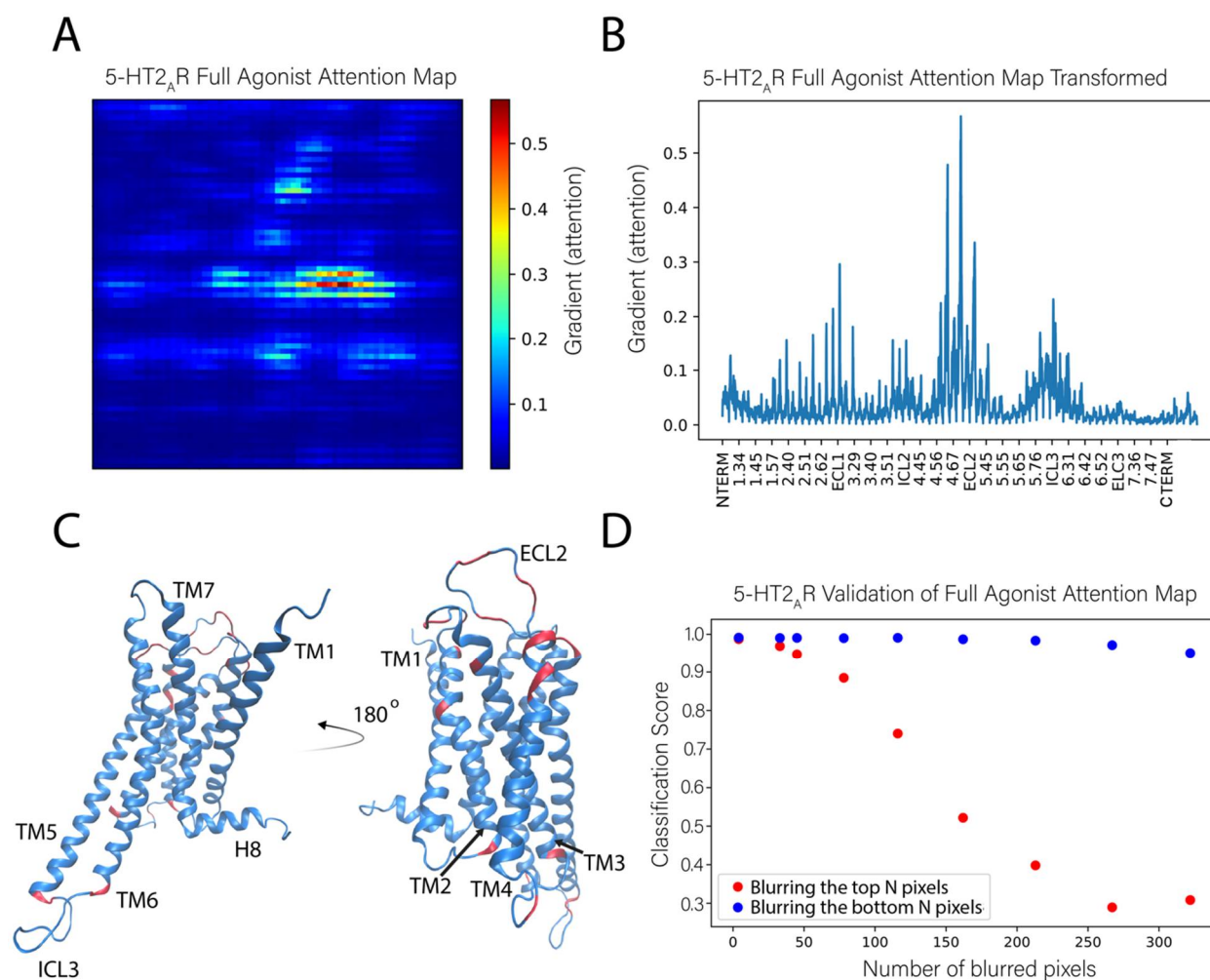
281

Figure 6: Identification of the molecular determinants of the classification of the full agonist bound to the 5-HT₂ₐR. **A:** The full agonist attention map shown was obtained as the average of 1000 attention maps calculated from 1000 instances of the full agonist bound to the 5-HT₂ₐR. **B:** Representation of the (average) attention map in panel A in which all the pixels (*i.e.*, atoms) are listed on the X axis. The tick marks on the X axis identify residues labeled with the generic Ballesteros-Weinstein numbering[20]. The gradient values calculated for the classifier for individual atoms is on the Y axis; it indicate the order of importance (salience) of each atom for the classification. **C:** The positions of the most important residues for the classification are indicated (in orange) on the ribbon representation (in blue) of the 5-HT₂ₐR model structure. The highlighted residues contain atoms whose gradient (attention) is >0.15. **D:** Validation of the attention map by evaluation of the effect of blurring increasing numbers of pixels (atoms) in the representation of the protein complex. Orange dots indicate the results of blurring increasing numbers of pixels identified to have the lowest gradient (least important). Blue dots indicate the results of blurring pixels with the highest gradient (most important). The number of atoms blurred is shown on the X axis; the Y axis shows the corresponding classification score of full agonist for the blurred images.

To verify further the role of these specific structural motifs in the classification produced by the neural network, we compared the effect of blurring the pixels with the highest gradient (most important; salient) to those with the lowest gradient (unimportant). In this procedure, sets of pixels corresponding to a number N of least-important atoms for all classes, were blurred in the test set by replacing them with Gaussian noise. This erased the information that these pixels confer to the neural network. The classification score computed for such an altered image represents the probability of an image belonging to a particular class, and the sum over all classes is unity. The same blurring procedure was then repeated for the same number of pixels with the highest gradient (importance) for a particular class.

306   The results of this analysis for the full agonist-bound class (in **Figure 6D),** show that when the
307   most important pixels are blurred (blue dots), the classification score quickly decreases to the chance
308   rate (~0.33 for 3 classes) with 250 blurred pixels. This means that the network is no longer able to
309   identify this instance as bound to full agonist. However, after blurring the same and even larger
310   numbers of unimportant pixels (orange dots), the neural network is still able to identify the instance
311   as belonging to the full agonist bound class (with a classification score >0.9).

312   *2.3.2 Sensitivity analysis applied to the classification of the D2R complexes*
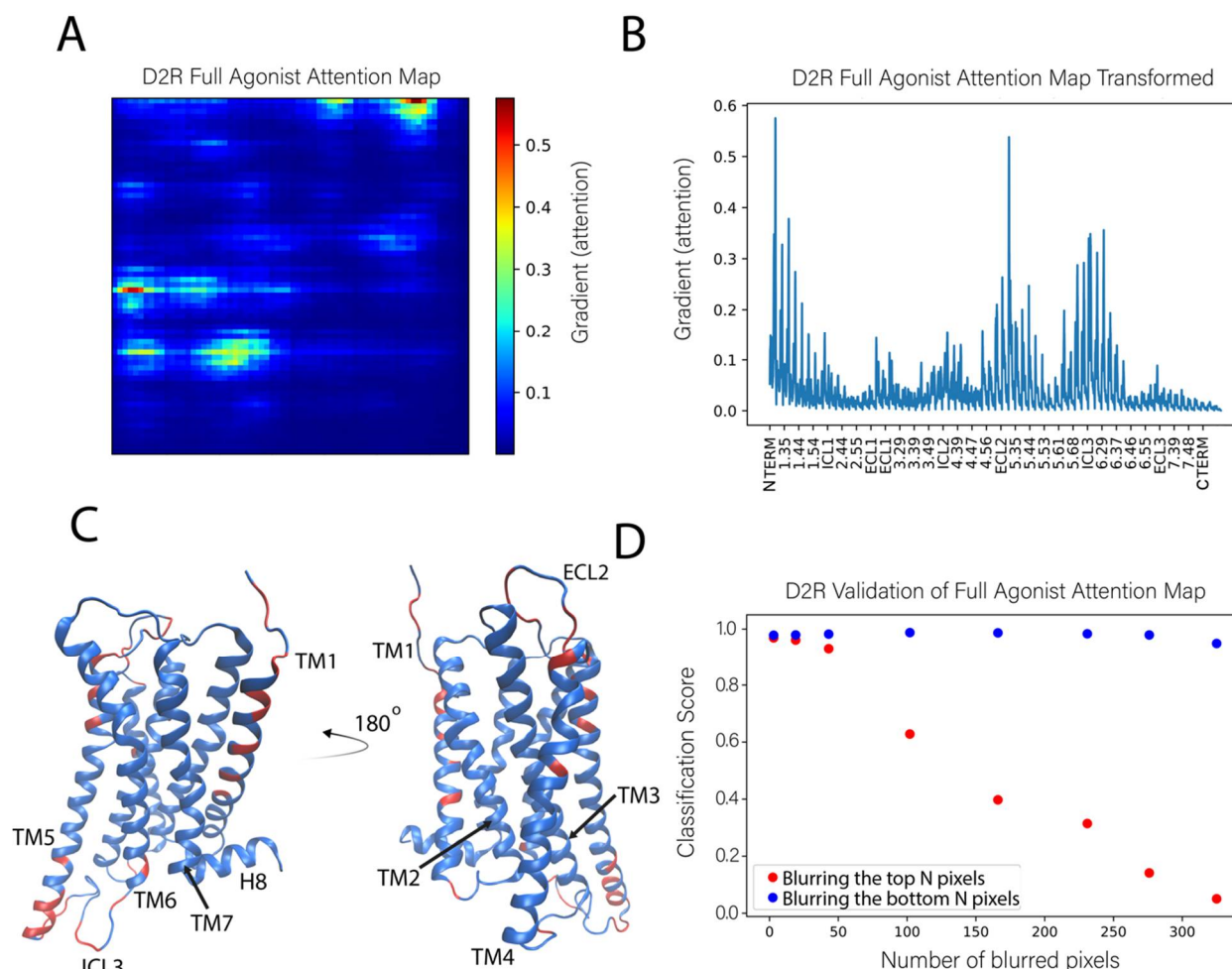

313

314   **Figure 7: Identification of the molecular determinants of the classification of the full agonist**
315   **bound to the D2R**. **A:** The full agonist attention map shown was obtained as the average of 1000
316   attention maps calculated from 1000 instances of the full agonist bound to the D2R. **B:** Representation
317   of the (average) attention map in panel A represented as in figure 6B. **C:** The positions of the most
318   important residues for the classification are indicated (in orange) on the ribbon representation (in
319   blue) of the D2R model structure. The highlighted residues contain atoms whose gradient (attention)
320   is >0.15. **D:** Validation of the attention map following the same procedure as described in figure 6D.

321   The results of applying the sensitivity analysis to the pharmacological classification of ligand-
322   bound complexes of the other class-A GPCR, D2R, shown in **Figure 4B**, are summarized in **Figure 7.**
323   Using the same importance cutoff value of 0.15 as in the analysis of the 5-HT$_{2A}$R, we find that the
324   most important residues in the classification of the ligand-D2R complexes reside in the middle and
325   the extracellular ends of TMs 1, 4, and 5 (positions 1.29, 1.30, 1.33, 1.34, 1.37, 1.38, 1.42, 1.46, 1.51, 4.53,
326   4.62, 5.35, 5.36, 5.39, 5.40, and 5.44), at the intracellular ends of TMs 5-6 (positions 5.64, 5.69, 5.70, 5.72-
327   5.74, 6.29, and 6.33) and in the extracellular loop ECL2, as well as intracellular loops ICL2 and ICL3.
328   These sites are indicated on the D2R structure in **Figure 7C**. There is some striking overlap between

329 the most important residues found by the attention map analyses of the D2R and 5-HT2ᴀR
330 trajectories. Among the most important regions found by both analyses was the intracellular ends of
331 TM5 and TM6, the extracellular end of TM4 and TM5, as well as ECL2, ICL2, and ICL3. Remarkably,
332 among the most important residues of both analyses was residues 4.62 and 5.36 on the extracellular
333 ends of TM4 and TM5, respectively. Multiple analogous residues of the ECL2 as well were identified
334 in both analyses, including the highly conserved cysteine (C227 in 5-HT2ᴀR and C182 in D2R) that
335 makes a disulfide bond with C3.25 and was shown to be critically important to the function of many
336 class A GPCRs[21].

337 *2.4 Dynamic differences discriminated by the DNN in the regions most important*
338 *for the classification decisions of ligand-bound GPCRs*

339   To gain additional insight into the nature of dynamic differences discriminated by the DNN in
340 the regions most important for the classification decisions, we compared the conformational
341 dynamics of specific residues identified by the atoms with high importance for the classification.

342 *2.4.1 5-HT₂ᴀR complexes*

343 Starting with the most important region identified in **Figure 6B**, *i.e.*, the second extracellular loop
344 (ECL2), we evaluated the dynamic range of the top hit of the sensitivity analysis for the 5-HT2ᴀR
345 bound to the full agonist, compared to the aligned trajectories of the 5-HT2ᴀR complex with a full
346 agonist and the inverse agonist. **Figure 8A** shows the sampling of the *epsilon* carbon (Cε) atom of F222
347 in ECL2. Although the starting structures of the GPCR in all 5-HT2ᴀR-ligand bound complexes were
348 highly similar (see Methods for details on docking), the conformational space sampled by this region
349 diverged over the course of the simulations. As **Figure 8A** shows,   ECL2 of the 5-HT2ᴀR bound to
350 the inverse agonist (KET) samples two distinct states over the trajectories in the dataset (red and
351 orange points in Figure 7A), with the red points indicating conformations in which F222 is almost
352 exclusively pointing inward, towards the binding pocket and TMs 6 and 7 (see Figure 8B bottom left).
353 In the other trajectory (orange points) of the KET-bound 5-HT2ᴀR, a section of the ECL2 including
354 F222 prefers an alpha-helical conformation, resulting in F222 pointing mostly away from the binding
355 pocket towards the extracellular side (Figure 8B top left), with some brief overlap with the sampling
356 of the red trajectory. Notably, both of these conformations are distinct from those sampled by the 5-
357 HT2ᴀR bound to the full agonist 5-HT (blue and purple points in Figure 8A). In the 5-HT-bound
358 trajectories, the section of the ECL2 containing F222 samples disordered/unfolded conformations in
359 which F222 primarily occupies a region of space away from the binding pocket than the KET-bound
360 (orange) trajectory, but shifted closer to TMs 1 and 2. Interestingly, in the trajectories of the 5-HT2ᴀR
361 bound to partial agonists, the Cε of F222 samples regions of space that overlap with both of the
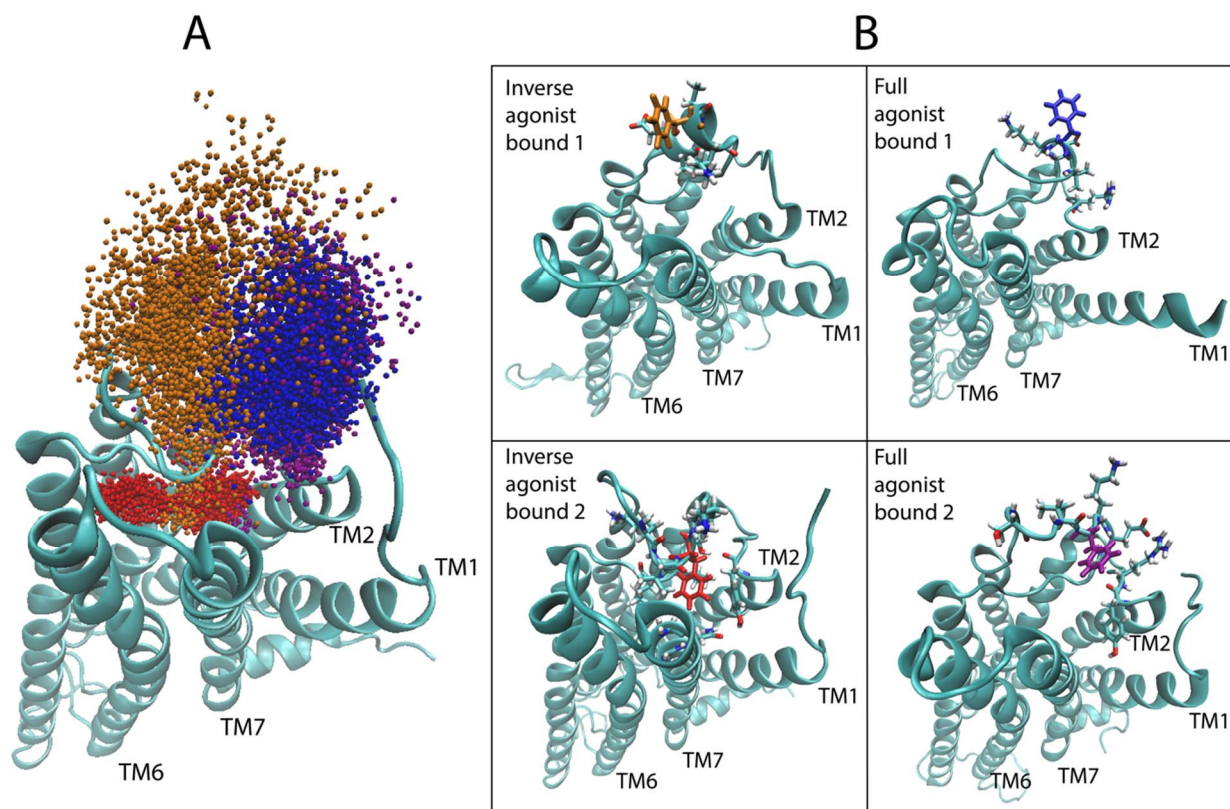362 regions sampled in the trajectories of the 5-HT2ᴀR bound to full and inverse agonist.

363

364

Figure 8. Conformational dynamics of residue F222 in ECL2 identified by the positions of the *epsilon* carbon atom Cε of F222 in the simulation trajectories. A. Sampling of the coordinates of Cε of F222 (atom 2532), the top hit of the sensitivity analysis for serotonin (5-HT), in the aligned trajectories of the 5-HT₂ₐR bound to the inverse agonist ketanserin (KET) (red and orange) and the full agonist 5-HT (blue and purple). **B.** Representative frames from each of the four trajectories shown in the previous panel. F222 is colored solidly according to the bound ligand, ketanserin (red and orange) and serotonin (blue and purple)

On the intracellular side of the receptor, we followed the conformational dynamics of residue R310 in ICL3, containing the *epsilon* hydrogen (Hε) identified as a highly salient atom. **Figure 9A** shows the sampling of the Hε in the aligned trajectories of the 5-HT₂ₐR bound to full 5-HT (in blue) and KET (in red). The two representative frames from the trajectories, shown in **Figure 9B,** illustrate the conformation of the ICL3 sampled by each class. There is near perfect separation between the space sampled by the Hε atom of R310 over the full and inverse agonist bound trajectories, confirming that this residue, identified as important by the neural network, indeed confers a large amount of information about whether and how the ensembles of ligand-dependent conformations differ.
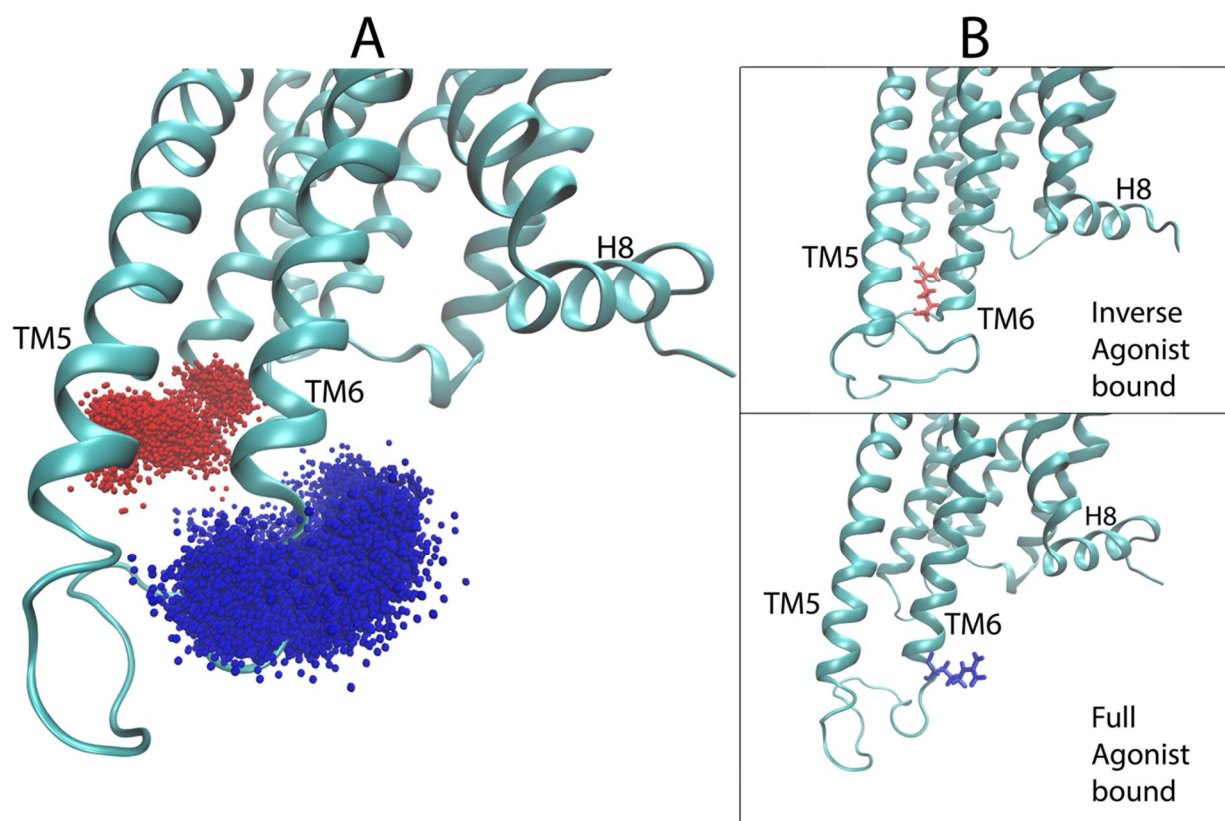
Figure 9. Conformational dynamics of residue R310 in ICL3 identified by the *epsilon* hydrogen highlighted by the sensitivity analysis. **A.** Sampling of the coordinate of the epsilon hydrogen of R310 (atom 3535) in the ICL3, over all of the aligned trajectories of the 5-HT2AR bound to the inverse agonist ketanserin (red) and the full agonist serotonin (blue). **B.** Example frames from each class of trajectories shown in panel A. R310 is colored solidly according to the bound ligand, KET (red) and 5-HT (blue)

The conformations of the partial agonist trajectories are differentiated by a different set of residues. The ICL3 of the partial agonist is not differentiated by the R310 Hε, as in the partial agonist-GPCR complex this atom samples both of the spaces shown in **Figure 9A**, with some preference for the trajectory of the full agonist. Instead, **Figure 10** shows that the conformation of the ICL3 in the partial agonist trajectories is different from the other complexes in that it preserves throughout the helical structure of the residue segment 306 to 310 of TM6, whereas the same piece of ICL3 samples a disordered/unfolded conformation in both the full and inverse agonist-bound trajectories (shown in Figure 9). This is evidenced by the sampling of T307 in the ICL3, a residue identified as important in the attention map of the partial agonist, but not the full agonist.
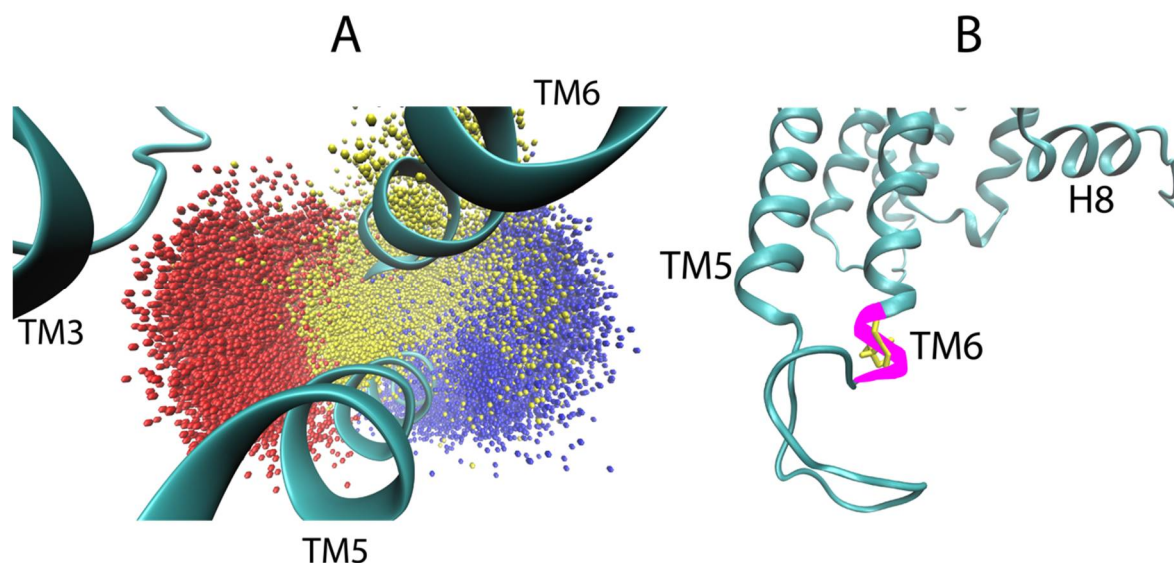
399

Figure 10. **Conformation of the ICL3 of the 5-HT₂ₐR in complexes with full- partial- and inverse-agonists.** In most of the partial agonist trajectories, a piece of the ICL3 (magenta) forms an extra helical turn of TM6. In the full and inverse agonist-bound trajectories, this piece of the ICL3 is disordered/unfolded, with T307 pointing inwards towards TM3 in the inverse agonist trajectories, and pointing away from TM3 in the full agonist bound trajectories. **A.** The sampling of the coordinate of the gamma oxygen of T307, an atom identified as important in the attention map of the partial agonist, for all the trajectories of the 5-HT₂ₐR bound to full agonist (in blue), inverse agonist (red), and partial agonist (yellow). **B.** Illustrative frame from partial agonist bound trajectories showing the extended helical conformation of the ICL3. T307 is colored in yellow and the extra helical turn is colored in magenta.

2.4.2 D2R complexes

For the dopamine receptor complexes we again focused first on ECL2 which was identified as important for the classification of the ligand-D2R complexes. **Figure 11A** shows the time dependence in the trajectory of the values taken by the dihedral angle across the disulfide bond formed between C182 in the loop and C3.25 (in TM3) over the full-agonist (DA) bound and inverse agonist (SLP) bound trajectories of the D2R. For the majority of the SLP-bound trajectories, the ECL2 samples conformations that are never sampled in the DA-bound trajectories. This is evidenced in the figure by the difference in the dihedral angle of the disulfide bond between the two cysteines. The DA trajectories (blue**)** remain in an angle range around -100°, never sampling above -40°, whereas the SLP (red) trajectory samples mostly around 100°. A simple cutoff of 0°, for example, can distinguish a majority of the inverse agonist frames. These differences in angle values determine different 3D orientations of the ECL2 which thus becomes a salient feature for describing the differences in the ensemble of conformations sampled by the trajectories of D2R bound to the full and inverse agonist.
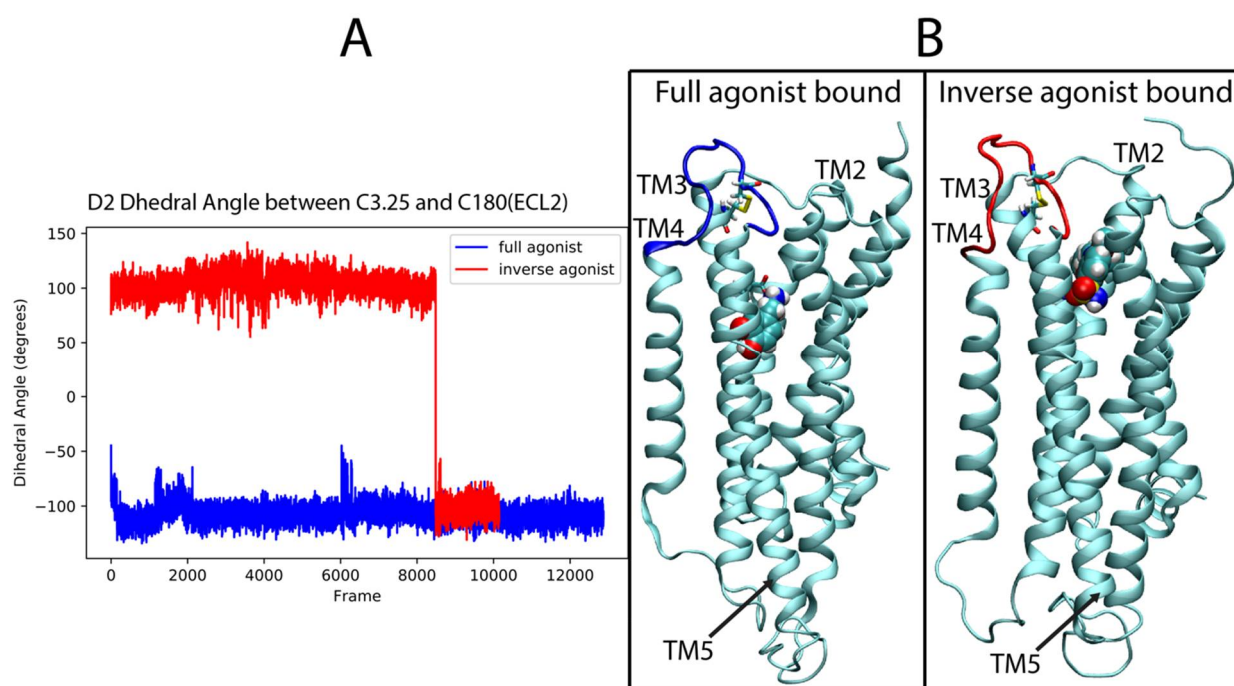
423

Figure 11: Involvement of residue C182 identified by the D2R sensitivity analysis in the discrimination of ECL2 structures. **A:** The dihedral angle is measured along the disulfide bond between C182 and C3.25 for the full agonist bound (blue) and inverse agonist bound (red) trajectories. **B:** Illustrative frames from the trajectories in panel A representing the two dihedral angle states. The ligand for each class (Dopamine for full agonist, and Sulpiride for the inverse agonist) is shown in function colored CPK.

Like in the 5-HT$_{2A}$R complexes, the residues in the extensions of TM5 and TM6 are important for the classification by the DNN. For the dynamic context, we compared residues K5.70 and T5.74 (both identified as important by the D2R sensitivity analysis) of the extension of TM5 in the aligned trajectories of the ligand-D2R complexes. Interestingly, inspection of the trajectories shows a difference in the preference of helical conformation of the intracellular end of TM5 dependent on the backbone hydrogen bond between these residues. The full-agonist bound trajectories preferred the helical conformation while the inverse-agonist bound trajectories preferred a disordered conformation. **Figure 12A** shows a measure of the helicity involving residues K5.70-T5.74 in the trajectories, quantified by the distance between the backbone oxygen of K5.70 and the backbone amide hydrogen of T5.74. The majority of frames in the DA-bound trajectories exhibit a smaller distance than those of the SLP-bound trajectories, because K5.70 and T5.74 form part of a helical structure for most of the full agonist trajectory, whereas in the inverse agonist bound trajectories these residues are in a more disordered conformation. **Figure 12B** presents example frames from the ensemble of conformations sampled by D2R bound to the full and inverse agonist, underscoring the clear difference in helicity of the TM5 region and thus the structural context of the identified importance of the two residues in the classification by the DNN.
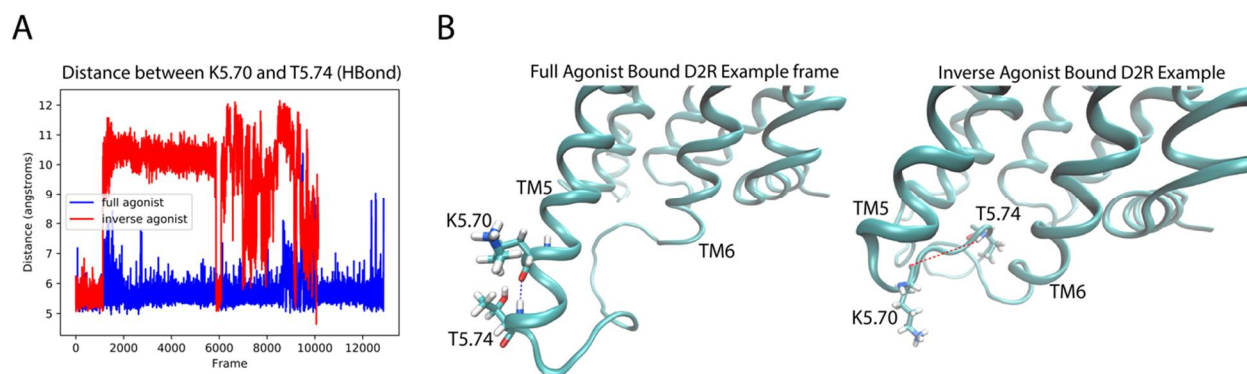
445

Figure 12: Residues K5.70 and T7.54 identified by the D2R sensitivity analysis determine the helicity of the intracellular TM5 extension. **A:** The distance between the backbone oxygen of K5.70 and the backbone amide hydrogen of T5.74 along trajectories of D2R bound to the full agonist (in blue) and the inverse agonist (red). **B:** Illustrative frames from the trajectories in panel A chosen for the distinct difference in the distance, and its effect on the helicity of the intracellular end of TM5.

3. Discussion

The machine learning-based approach we developed and illustrated here with applications to the classification of ligand-determined GPCR conformational properties, points to some new directions taken by methods for MD trajectory analysis. In particular, analyses involving machine learning are growing in popularity as a greater variety of scientific questions is being addressed with MD simulations, and the systems targeted are increasingly complex. The data generated by these ever larger scales of simulation, accrued for large systems that require longer simulation times, is moving the field into the realm of Big Data Science [22]. A recent review of fundamental MD problems that could be addressed in the framework of Machine Learning (ML) [23], shows how ML has the potential to tackle problems arising from large scale simulations, and that it has already had profound impact on alleviating them (see Noe *et al.*[23] and references therein).

The work we present supports the overall optimistic outlook regarding the potential of ML algorithms to extract important functional information from MD simulation trajectories in the usual structural and dynamic context of molecular mechanisms. An imperative in this respect, is the development of approaches to translate the results obtained with DNN-based protocols into clear structural information in order to illuminate the underlying mechanisms in a physics-based context. By extracting automatically the functional information we achieved a major reduction in dimensionality of MD Big Data into a collection of salient structural motifs that efficiently describe the differences between ensembles of conformations sampled by each tested state. The results of this study are particularly encouraging, despite the limited scope of the test framework used in the illustration, as the approaches (i)-classify correctly the ligand-bound GPCRs, (ii)-identify the molecular determinants of the classification, and thus also the dynamic differences in the regions most important for the classification decisions.

Only 5 ligands for the serotonin 5-HT$_{2A}$R and 3 for the dopamine D2 receptors were used in this limited test, but the results show that through the methodology described herein, a DNN is able to identify the relation between the functional properties of ligand-receptor complexes and the ensemble of conformations that they sample within MD trajectories. Due to the limited sampling of both configurational space and the classification field, the trajectory data served here only to exemplify the ability of the method to distinguish functional states of a GPCR, not to reach any conclusion about the significance of the functional states themselves. And yet, it is encouraging to observe that most of the salient regions for identifying the ligand-dependent conformational

484 differences are common to both the 5-HT$_{2A}$R and D2R, and are regions known to be important for
485 GPCR activation. Thus, the ECL2 has been shown to play a critical role in class A GPCR activation[24],
486 taking on ligand-dependent conformations that are important for function[24-27]. The regions of the
487 intracellular side of the receptor identified by our analysis, including the two ends of the ICL3 (*i.e.*,
488 the N-terminus of the loop which continues TM5, and its C-terminus which elongates the start of
489 TM6), are also critically important for GPCR activation as these sites directly interact with the G
490 protein[28] . As such, they are involved in the opening, observed in active GPCRs[29], of the
491 intracellular side of the receptor.

492   It is noteworthy, however, that while they serve to discriminate between ligand classes, the
493 dynamics of these salient motifs differ between the 5-HT$_{2A}$R and D2R systems. This is further
494 reassuring because even if their role in recognizing the G protein, say (for the ICL3 motifs) is the same,
495 they must respond to different G proteins in different functional contexts. However, that the
496 structural motifs mentioned above were similarly sensitive to the bound ligand in both systems is
497 concordant with the evidence that class A GPCRs involve similar structural motifs in the
498 pharmacological response. Collectively, the accuracy and agreement between the sensitivity analyses
499 applied to the 5-HT$_{2A}$R and D2R trajectories suggests that this method should generalize to other
500 GPCR simulation studies, including trajectories of other ligand-GPCR complexes in diverse coupling
501 pathways.

502   The characteristics of the novel method of analysis described here support its applicability not
503 just to classifications of receptor activity (efficacy), but by finding ligand-dependent differences in
504 MD trajectories of GPCRs, it is especially promising for the classification of ligand bias in functional
505 selectivity as well. Our ongoing work is exploring this application, as well other functional
506 classifications being studied such as membrane lipid composition or the presence or absence of an
507 action such as ion release.

508 **4. Materials and Methods**

509 *Building homology model of the GPCRs*

510   MODELLER (v.9.18)[30] was used to generate the sets of homology models of the human 5-
511 HT$_{2A}$R, and the human dopamine D2R. Briefly, Modeller generates 3D homology models of
512 proteins using sequence alignments between the target and homologous proteins, as well as
513 experimental structural data (*e.g.* x-ray or cryoEM structures from homologous proteins). These
514 models are generated by optimally satisfying spatial restraints that are derived from the template
515 structure(s). Because template-derived spatial constraints inform model construction, there is
516 tension between choosing the most homologous template structures and providing Modeller with a
517 set of template structures that possess enough sequential/structural heterogeneity so that the
518 resultant set of homology models are significantly structurally diverse.

519 *Modeling the 5-HT$_{2A}$R:* Three sets of sequence alignments/crystal structures were used as templates
520 in Modeller:

521 - Set 1 consisted of two structures of the human 5HT$_{2B}$R (PDBID: 4ib4 and 5tvn);

522 - Set 2: included two structures of the human 5HT$_{2B}$R (PDBID: 4ib4 and 5tvn) and

523 two structures of the human 5HT$_{1B}$R (PDBID: 4iaq and 4iar);

524 - Set 3: included all the structures in Set 2, augmented by 2 structures of the human ß2-
525   adrenergic receptor b2AR (PDBID: 4lde and 4ldl).

526 Each of these template structures includes the receptor bound to one of its agonists. For each
527 template set, Modeller was used to generate 1,000 homology models of the 5-HT$_{2A}$R.To select a
528 single homology model from the 3 sets of Modeller outputs, each model was evaluated for its

529   ability to discriminate between 5-HT$_{2A}$R agonists and decoy ligands (*i.e.* ligands that are predicted
530   to not bind 5-HT$_{2A}$R); this characterization was performed by employing a multistep procedure.

531   First, a set of 47 known human 5-HT$_{2A}$R agonists was obtained from the IUPHAR/BPS database
532   [accessed on May 1st, 2017] [31]. These agonists were then submitted to the DUD-E server [accessed
533   on May 5th, 2017] [32], which generated a set of 3,229 decoy structures. Briefly, DUD-E generates
534   decoy structures that have similar physical chemistry properties (*e.g.* molecular weight, hydrogen
535   bond donors/acceptors, rotatable bonds, *etc.*) but have a dissimilar topology. Schrodinger's LigPrep
536   software (v. 40015) was used to convert the agonist set and DUD-E SMILES descriptions into 3D
537   ligand models.

538   Next, the 3 sets of 1,000 Modeller homology models were prepared for docking studies using
539   Schrodinger's Protein Preparation Wizard (v. 2016-2) [33]; this procedure added hydrogen atoms
540   and created the disulfide bond between C3.25(148) and ECL2 loop residue C227. Schrodinger's
541   Glide software (v.34014) [34] was used to dock each of the 47 agonist and 3,229 decoy structures
542   into the models in the 3 sets (3,000 models total), using standard precision; for each receptor/ligand
543   complex, Glide calculates a 'GlideScore', which is an approximation of the ligand's free energy of
544   binding to the protein.

545   Each model's ability to discriminate between true agonist and decoy structures was quantified
546   using the set of ligand GlideScores. The set that only used 5HT$_{2B}$ as input templates was the most
547   discriminating model overall and was used for subsequent docking studies, described below.

548   *Molecular construct for D2R*

549   The crystal structure of the D2 dopamine receptor bound to Risperidone [27] was used as
550   starting construct. The missing intracellular loop IL2 was modelled using MODELLER [30]. The
551   long intracellular loop IL3, substituted by T4 lysozyme in the crystal construct, was replaced by a
552   10mer of Gly residues, inserted between S229 and Q365.

553   *Parametrization and docking of the molecular models*

554   MOL2 files for the 5-HT$_{2A}$R ligands (5-HT, Ketanserin, LSD, Lisuride, and DOI) as well as for
555   the D2R ligands (Dopamine, Sulpiride, Aripiprazole) were obtained from the ZINC [35] database.
556   The amide nitrogen in these compounds was protonated and docking poses were generated into
557   the identical 5-HT$_{2A}$R homology model and into the D2R structure using the Induced Fit [36-38]
558   protocol in the Schrodinger Suite. A starting binding pose was chosen for each ligand based on the
559   e-modal score and comparison to experimental data [25-27, 39-43]. Parameters for the CHARMM36
560   [44] force field each ligand were obtained by analogy from the CGenFF program [45, 46].
561   Parameters with analogy penalties greater than or equal to 5 were optimized using the Force Field
562   Toolkit (ffTK) [47]. Quantum mechanical calculations were made at the Hartree-Fock level of theory
563   using the Gaussian software [48].

564   *Molecular dynamics simulations*

565   The GPCR systems were simulated in atomistically explicit membrane environments following
566   established lab protocols (e.g., see REFs). For the simulation of 5-HT$_{2A}$R-ligand complexes the
567   molecular model was inserted into a membrane containing 144:16 POPC:Cholesterol molecules of
568   in each leaflet. The membranes were built using the CHARMM-GUI[49] and equilibrated using the
569   NAMD[50] software ver2.12 according to an equilibration protocol generated[51] by the
570   CHARMM-GUI. After inserting the protein into the equilibrated membrane, the protein-membrane
571   complex was surrounded by a 0.15 M NaCl solution with a hydration number of 80 water
572   molecules per lipid using the CHARMM-GUI. Similarly, for the D2R-ligand simulations the

573 structures were embedded, using the CHARMM-GUI, into a membrane consisting of 180:18
574 POPC:Cholesterol molecules per leaflet, and was solvated and ionized using the same conditions as
575 above.

576   Each complete system was equilibrated under the NPT ensemble (T=310K) in NAMD
577 according to a previously established multistep equilibration protocol [16, 52] before running
578 approximately 1.5 microsecond long trajectories for each under the NVT ensemble (T=310K). The
579 production runs were carried out with the ACEMD3 [53] software with a 4 femtosecond time-step
580 and with all the standard simulation parameters [5, 9, 16, 52] following established and
581 documented protocols (REFs as indicated).

582 *Machine Learning procedures*

583 *Building the DNN:* A custom Densely Connected Neural Network [15, 18] was constructed, with 4
584 dense blocks containing 6, 12, 36, and 24 layers, respectively, a growth rate of 48 filters per layer, 96
585 initial filters, and a reduction ratio of 0.5, in Keras [54] with a Tensorflow [55] backend based on an
586 established implementation [56]

587 *Classification of the trajectories:* Each frame of the scrambled trajectories was converted into a visual
588 representation using the previously-described algorithm. Each frame was assigned a label
589 according to its functional class (0 for full agonist bound, 1 for partial agonist bound, and 2 for
590 inverse agonist bound). The frames were randomly split into a training, validation, and test set in
591 the ratio of 56:24:20, respectively. The neural network was trained on the training and validation
592 sets, and tested on the test set. The reported score is based on the test set.

593 <u>*Sensitivity analysis (keras-vis):*</u>   The sensitivity analysis was performed by computing the gradient
594 using the visual saliency package provided by keras-vis [57] with guided back-propagation.

595

612

613 **Conflicts of Interest:** The authors declare no conflict of interest.

614

615   **References**

616   1.   Smith JS, Lefkowitz RJ, Rajagopal S. Biased signalling: from simple switches to allosteric microprocessors.
617   Nat Rev Drug Discov. 2018;17(4):243-60.

618   2.   Berg KA, Maayani S, Goldfarb J, Scaramellini C, Leff P, Clarke WP. Effector pathway-dependent relative
619   efficacy at serotonin type 2A and 2C receptors: evidence for agonist-directed trafficking of receptor stimulus.
620   Mol Pharmacol. 1998;54(1):94-104.

621   3.   Urban JD, Clarke WP, von Zastrow M, Nichols DE, Kobilka B, Weinstein H, et al. Functional selectivity and
622   classical concepts of quantitative pharmacology. J Pharmacol Exp Ther. 2007;320(1):1-13.

623   4.   Weinstein H. Hallucinogen actions on 5-HT receptors reveal distinct mechanisms of activation and
624   signaling by G protein-coupled receptors. Aaps Journal. 2005;7(4):E871-E84.

625   5.   Shan JF, Khelashvili G, Mondal S, Mehler EL, Weinstein H. Ligand-Dependent Conformations and
626   Dynamics of the Serotonin 5-HT2A Receptor Determine Its Activation and Membrane-Driven Oligomerization
627   Properties. Plos Computational Biology. 2012;8(4).

628   6.   Wingler LM, Elgeti M, Hilger D, Latorraca NR, Lerch MT, Staus DP, et al. Angiotensin Analogs with
629   Divergent Bias Stabilize Distinct Receptor Conformations. Cell. 2019;176(3):468-+.

630   7.   Perez-Aguilar JM, Shan JF, LeVine MV, Khelashvili G, Weinstein H. A Functional Selectivity Mechanism
631   at the Serotonin-2A GPCR Involves Ligand-Dependent Conformations of Intracellular Loop 2. Journal of the
632   American Chemical Society. 2014;136(45):16044-54.

633   8.   Hollingsworth SA, Dror RO. Molecular Dynamics Simulation for All. Neuron. 2018;99(6):1129-43.

634   9.   Razavi AM, Khelashvili G, Weinstein H. A Markov State-based Quantitative Kinetic Model of Sodium
635   Release from the Dopamine Transporter. Sci Rep. 2017;7:40076.

636   10.   Song X, Jensen MO, Jogini V, Stein RA, Lee CH, McHaourab HS, et al. Mechanism of NMDA receptor
637   channel block by MK-801 and memantine. Nature. 2018;556(7702):515-9.

638   11.   Shaw DE, Dror RO, Salmon JK, Grossman JP, Mackenzie KM, Bank JA, et al. Millisecond-Scale Molecular
639   Dynamics Simulations on Anton. Proceedings of the Conference on High Performance Computing Networking,
640   Storage and Analysis. 2009.

641   12.   Motlagh HN, Wrabl JO, Li J, Hilser VJ. The ensemble nature of allostery. Nature. 2014;508(7496):331-9.

642   13.   Chen M, Mao SW, Liu YH. Big Data: A Survey. Mobile Netw Appl. 2014;19(2):171-209.

643   14.   Frankel F, Reid R. Big data: Distilling meaning from data. Nature. 2008;455(7209):30-.

644   15.   Huang G, Liu Z, van der Maaten L, Weinberger KQ. Densely Connected Convolutional Networks. Proc
645   Cvpr Ieee. 2017:2261-9.

646   16.   Khelashvili G, Stanley N, Sahai MA, Medina J, LeVine MV, Shi L, et al. Spontaneous inward opening of the
647   dopamine transporter is triggered by PIP2-regulated dynamics of the N-terminus. ACS Chem Neurosci.
648   2015;6(11):1825-37.

649   17.   LeVine MV, Weinstein H. NbIT - A New Information Theory-Based Analysis of Allosteric Mechanisms
650   Reveals Residues that Underlie Function in the Leucine Transporter LeuT. Plos Computational Biology.
651   2014;10(5).

652   18.   Pleiss G, Chen D, Huang G, Li T, van der Maaten L, Weinberger KQ. Memory-efficient implementation of
653   densenets. arXiv preprint arXiv:170706990. 2017.

654   19.   Karen Simonyan AV, Andrew Zisserman. Deep Inside Convolutional Networks: Visualising Image
655   Classification Models and Saliency Maps. ICLR. 2013.

656 20. Ballesteros J, Weinstein, H. Integrated methods for the construction of three-dimensional models and
657   computational probing of structure-function relations in G protein-coupled receptors. Methods in
658   Neurosciences. 1995;25:366-428.

659 21. Venkatakrishnan AJ, Deupi X, Lebon G, Tate CG, Schertler GF, Babu MM. Molecular signatures of G-
660   protein-coupled receptors. Nature. 2013;494(7436):185-94.

661 22. Yu I, Feig M, Sugita Y. High-Performance Data Analysis on the Big Trajectory Data of Cellular Scale All-
662   atom Molecular Dynamics Simulations. J Phys Conf Ser. 2018;1036.

663 23. Noé F. Machine Learning for Molecular Dynamics on Long Timescales. arXiv. 2018.

664 24. Wheatley M, Wootten D, Conner MT, Simms J, Kendrick R, Logan RT, et al. Lifting the lid on GPCRs: the
665   role of extracellular loops. Brit J Pharmacol. 2012;165(6):1688-703.

666 25. Peng Y, McCorvy JD, Harpsoe K, Lansu K, Yuan S, Popov P, et al. 5-HT2C Receptor Structures Reveal the
667   Structural Basis of GPCR Polypharmacology. Cell. 2018;172(4):719-30 e14.

668 26. Wacker D, Wang S, McCorvy JD, Betz RM, Venkatakrishnan AJ, Levit A, et al. Crystal Structure of an LSD-
669   Bound Human Serotonin Receptor. Cell. 2017;168(3):377-89 e12.

670 27. Wang S, Che T, Levit A, Shoichet BK, Wacker D, Roth BL. Structure of the D2 dopamine receptor bound to
671   the atypical antipsychotic drug risperidone. Nature. 2018;555(7695):269-73.

672 28. Flock T, Hauser AS, Lund N, Gloriam DE, Balaji S, Babu MM. Selectivity determinants of GPCR-G-protein
673   binding. Nature. 2017;545(7654):317-+.

674 29. Katritch V, Cherezov V, Stevens RC. Structure-function of the G protein-coupled receptor superfamily.
675   Annu Rev Pharmacol Toxicol. 2013;53:531-56.

676 30. Webb B, Sali A. Protein Structure Modeling with MODELLER. Methods Mol Biol. 2017;1654:39-54.

677 31. Harding SD, Sharman JL, Faccenda E, Southan C, Pawson AJ, Ireland S, et al. The IUPHAR/BPS Guide to
678   PHARMACOLOGY in 2018: updates and expansion to encompass the new guide to
679   IMMUNOPHARMACOLOGY. Nucleic Acids Research. 2018;46(D1):D1091-D106.

680 32. Mysinger MM, Carchia M, Irwin JJ, Shoichet BK. Directory of useful decoys, enhanced (DUD-E): better
681   ligands and decoys for better benchmarking. J Med Chem. 2012;55(14):6582-94.

682 33. Sastry GM, Adzhigirey M, Day T, Annabhimoju R, Sherman W. Protein and ligand preparation:
683   parameters, protocols, and influence on virtual screening enrichments. J Comput Aided Mol Des. 2013;27(3):221-
684   34.

685 34. Friesner RA, Murphy RB, Repasky MP, Frye LL, Greenwood JR, Halgren TA, et al. Extra precision glide:
686   docking and scoring incorporating a model of hydrophobic enclosure for protein-ligand complexes. J Med
687   Chem. 2006;49(21):6177-96.

688 35. Irwin JJ, Sterling T, Mysinger MM, Bolstad ES, Coleman RG. ZINC: a free tool to discover chemistry for
689   biology. J Chem Inf Model. 2012;52(7):1757-68.

690 36. Sherman W, Beard HS, Farid R. Use of an induced fit receptor structure in virtual screening. Chem Biol
691   Drug Des. 2006;67(1):83-4.

692 37. Sherman W, Day T, Jacobson MP, Friesner RA, Farid R. Novel procedure for modeling ligand/receptor
693   induced fit effects. Journal of Medicinal Chemistry. 2006;49(2):534-53.

694 38. Farid R, Day T, Friesner RA, Pearlstein RA. New insights about HERG blockade obtained from protein
695   modeling, potential energy mapping, and docking studies. Bioorgan Med Chem. 2006;14(9):3160-73.

696 39. Braden MR, Parrish JC, Naylor JC, Nichols DE. Molecular interaction of serotonin 5-HT2A receptor
697   residues Phe339((6.51)) and Phe340((6.52)) with superpotent N-benzyl phenethylamine agonists. Molecular
698   Pharmacology. 2006;70(6):1956-64.

699   40.   Almaula N, Ebersole BJ, Zhang DQ, Weinstein H, Sealfon SC. Mapping the binding site pocket of the
700   serotonin 5-hydroxytryptamine(2A) receptor - Ser(3.36(159)) provides a second interaction site for the
701   protonated amine of serotonin but not of lysergic acid diethylamide or bufotenin. Journal of Biological
702   Chemistry. 1996;271(25):14672-5.

703   41.   Sealfon SC, Chi L, Ebersole BJ, Rodic V, Zhang D, Ballesteros JA, et al. Related Contribution of Specific
704   Helix-2 and Helix-7 Residues to Conformational Activation of the Serotonin 5-Ht2a Receptor. Journal of
705   Biological Chemistry. 1995;270(28):16683-8.

706   42.   Michino M, Free RB, Doyle TB, Sibley DR, Shi L. Structural basis for Na+-sensitivity in dopamine D2 and
707   D3 receptors. Chem Commun. 2015;51(41):8618-21.

708   43.   Kling RC, Tschammer N, Lanig H, Clark T, Gmeiner P. Active-State Model of a Dopamine D-2 Receptor -
709   G alpha(i) Complex Stabilized by Aripiprazole-Type Partial Agonists. Plos One. 2014;9(6).

710   44.   Vanommeslaeghe K, Hatcher E, Acharya C, Kundu S, Zhong S, Shim J, et al. CHARMM general force field:
711   A force field for drug-like molecules compatible with the CHARMM all-atom additive biological force fields. J
712   Comput Chem. 2010;31(4):671-90.

713   45.   Vanommeslaeghe K, MacKerell AD, Jr. Automation of the CHARMM General Force Field (CGenFF) I: bond
714   perception and atom typing. J Chem Inf Model. 2012;52(12):3144-54.

715   46.   Vanommeslaeghe K, Raman EP, MacKerell AD, Jr. Automation of the CHARMM General Force Field
716   (CGenFF) II: assignment of bonded parameters and partial atomic charges. J Chem Inf Model. 2012;52(12):3155-
717   68.

718   47.   Mayne CG, Saam J, Schulten K, Tajkhorshid E, Gumbart JC. Rapid Parameterization of Small Molecules
719   Using the Force Field Toolkit. Journal of Computational Chemistry. 2013;34(32):2757-70.

720   48.   M. J. Frisch GWT, H. B. Schlegel, G. E. Scuseria, M. A. Robb, J. R. Cheeseman, G. Scalmani, V. Barone, G.
721   A. Petersson, H. Nakatsuji, X. Li, M. Caricato, A. Marenich, J. Bloino, B. G. Janesko, R. Gomperts, B. Mennucci,
722   H. P. Hratchian, J. V. Ortiz, A. F. Izmaylov, J. L. Sonnenberg, D. Williams-Young, F. Ding, F. Lipparini, F. Egidi,
723   J. Goings, B. Peng, A. Petrone, T. Henderson, D. Ranasinghe, V. G. Zakrzewski, J. Gao, N. Rega, G. Zheng, W.
724   Liang, M. Hada, M. Ehara, K. Toyota, R. Fukuda, J. Hasegawa, M. Ishida, T. Nakajima, Y. Honda, O. Kitao, H.
725   Nakai, T. Vreven, K. Throssell, J. A. Montgomery, Jr., J. E. Peralta, F. Ogliaro, M. Bearpark, J. J. Heyd, E. Brothers,
726   K. N. Kudin, V. N. Staroverov, T. Keith, R. Kobayashi, J. Normand, K. Raghavachari, A. Rendell, J. C. Burant, S.
727   S. Iyengar, J. Tomasi, M. Cossi, J. M. Millam, M. Klene, C. Adamo, R. Cammi, J. W. Ochterski, R. L. Martin, K.
728   Morokuma, O. Farkas, J. B. Foresman, and D. J. Fox. Gaussian 09, Revision B.01. G09, Revision B.01 ed: Gaussian,
729   Inc; 2009.

730   49.   Jo S, Kim T, Iyer VG, Im W. CHARMM-GUI: a web-based graphical user interface for CHARMM. J Comput
731   Chem. 2008;29(11):1859-65.

732   50.   Phillips JC, Braun R, Wang W, Gumbart J, Tajkhorshid E, Villa E, et al. Scalable molecular dynamics with
733   NAMD. J Comput Chem. 2005;26(16):1781-802.

734   51.   Lee J, Cheng X, Jo S, MacKerell AD, Klauda JB, Im W. CHARMM-GUI Input Generator for NAMD,
735   Gromacs, Amber, Openmm, and CHARMM/OpenMM Simulations using the CHARMM36 Additive Force Field.
736   Biophysical Journal. 2016;110(3):641a-a.

737   52.   Shi L, Quick M, Zhao Y, Weinstein H, Javitch JA. The mechanism of a neurotransmitter:sodium symporter-
738   -inward release of Na+ and substrate is triggered by substrate in a second binding site. Mol Cell. 2008;30(6):667-
739   77.

740   53.   Harvey MJ, Giupponi G, De Fabritiis G. ACEMD: Accelerating Biomolecular Dynamics in the Microsecond
741   Time Scale. Journal of Chemical Theory and Computation. 2009;5(6):1632-9.

742   54.   Chollet F. keras, Github. 2015.

743   55.   Martín Abadi AA, Paul Barham, Eugene Brevdo,, Zhifeng Chen CC, Greg S. Corrado, Andy Davis,, Jeffrey

744   Dean MD, Sanjay Ghemawat, Ian Goodfellow,, Andrew Harp GI, Michael Isard, Rafal Jozefowicz, Yangqing Jia,,

745   Lukasz Kaiser MK, Josh Levenberg, Dan Mané, Mike Schuster,, Rajat Monga SM, Derek Murray, Chris Olah,

746   Jonathon Shlens,, et al. TensorFlow: Large-scale machine learning on heterogeneous systems. 2015.

747   56.   Yu) FF. DenseNet-Keras. Github; 2017.

748   57.   Kotikalapudi Rac. keras-vis. GitHub; 2017.

749